Evaluation of a PtSi Schottky infrared CCD for astronomy

Eustace L. Dereniak, J. P. Britt, A. M. Fowler, R. R. Joyce, G. Boreman, and William S. Ewing

This paper presents the results of a preliminary evaluation of a platinum silicide (PtSi) Schottky CCD as an imaging array for astronomical applications. The work was done in the near-infrared ($1.2\ \mu m < \lambda < 2.5\ \mu m$) spectral regime, where there is presently a lack of commercially available panoramic arrays with acceptable performance. During an initial test run, the array detected a star of magnitude 3.5 using an integration time of 128 msec. Proper optimization of the readout electronics, cryostat configuration, and matching of the telescope image scale to the pixel size could allow detection of a source ~100 times fainter in a 1-sec integration time. This paper will discuss the array architecture, measurement and signal processing techniques, and the observatory and laboratory evaluation tests.

I. PtSi Schottky Array Architecture

The infrared (IR) focal plane is a monolithic array of 32×64 platinum silicide (PtSi) diodes on a p-type silicon substrate that was designed by Walter Kosonocky of RCA, Princeton, N.J.[1–3] The PtSi Schottky diodes are made by evaporating a pattern of platinum on the p-type silicon substrate followed by an annealing process to form the silicide compound. The detection of IR radiation occurs[1,4,5] within the resulting PtSi Schottky barrier diodes. In addition to the detectors, the focal plane has a buried channel CCD shift register and amplifier for signal readout.[6]

The PtSi diodes are back-illuminated, so the incident radiation must pass through the silicon substrate to reach the detectors.[5] Therefore, the cut-on wavelength of the device is 1.1 μm due to the blocking action of the silicon substrate, whereas the cutoff wavelength is controlled by the metal-semiconductor Schottky barrier as shown in Eq. (1):

$$\lambda = \frac{1.24}{\psi_{\text{msec}}}, \tag{1}$$

where λ is the cutoff wavelength in micrometers, and ψ_{msec} is the Schottky barrier potential in electron volts. Thus photons with energies lying within this spectral band produce electrons by means of an internal photoelectric effect. The quantum yield $Y(h\nu)$ is determined by ψ_{msec} and the quantum efficiency coefficient C_1 and is defined by the modified Fowler equation[7]:

$$Y(h\nu) = \frac{C_1}{h\nu}(h\nu - \psi_{\text{msec}})^2, \tag{2}$$

with $h\nu$ in electron volts and C_1 in (electron volts).$^{-1}$ Rearranging terms results in an expression that shows the spectral response in terms of the cutoff wavelength λ_c:

$$Y(h\nu) = 1.24\frac{C_1}{\lambda}\left(1 - \frac{\lambda}{\lambda_c}\right)^2. \tag{3}$$

The IR detection process occurs by internal photoemission, and its efficiency depends in part on the thickness of the PtSi layer.[8] The IR photon is absorbed in the PtSi layer, producing an electron whose energy is above the Fermi level and the creation of a hole below the Fermi level. If the hole energy is below the Schottky barrier potential ψ_{msec}, an electron from the semiconductor can tunnel into the silicide to fill this vacancy. The energy band diagram depicting this process is shown in Fig. 1. In the operation of this array, the PtSi layer is floating at a preset bias above the substrate during the photodetection process, so the net effect of the photoemission process is to increase the number of electrons on the PtSi, thus reducing its potential. Blooming due to a strong flux input is effectively controlled, since an excess accumulation of negative charge forward biases the junction and prevents further photoemission. The resulting forward bias is not sufficient to inject charge into the CCD register, thereby localizing the saturation and preventing the blooming common to CCD type detector arrays.

The focal plane assembly is an interline transfer[9] type device with 32 columns of 64 detectors in a square format. Figure 2 is a partial array showing five columns and six rows to illustrate the architecture. The CCD shift registers are of the four-phase design with the horizontal register containing an extra transfer cell between each column. This is necessary to accommo-

William Ewing is with Rome Air Development Center/ESE, Hanscom AFB, Bedford, Massachusetts 01731; G. Boreman and E. L. Dereniak are with University of Arizona, Optical Sciences Center, Tucson, Arizona 85721; and the other authors are with Kitt Peak National Observatory, Tucson, Arizona 85726.

Received 23 July 1983.

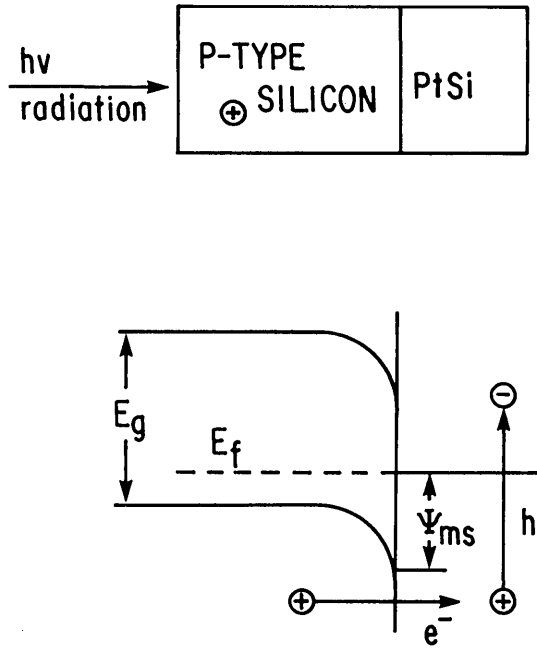

Fig. 1. Energy band diagram of PtSi Schottky barrier detector. E_g is the intrinsic energy gap in the silicon substrate, and E_f is the Fermi level.

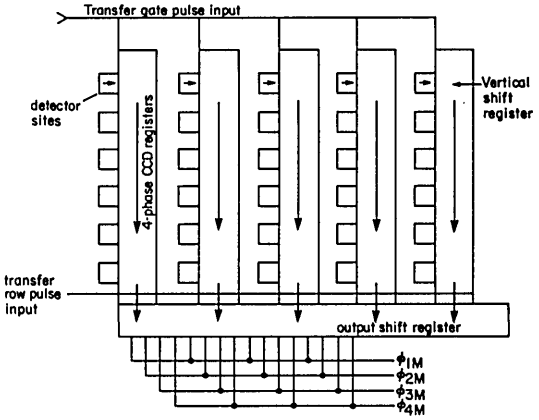

Fig. 2. Partial layout of interline transfer focal plane.

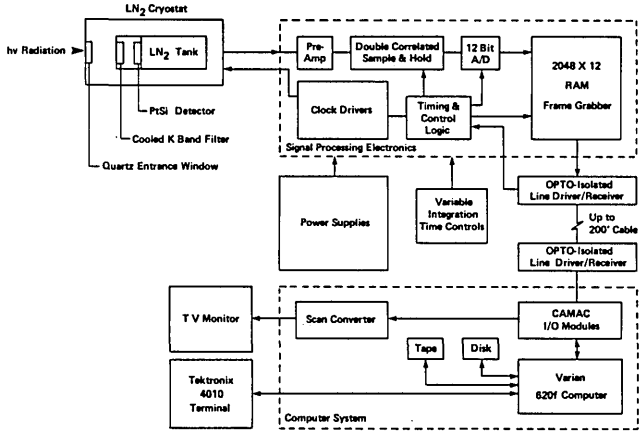

Fig. 3. Block diagram of general test geometry.

date the extra space between columns due to the vertical shift register. These dummy pixels are interlaced on the output video with valid picture information. This feature may be of great value in overcoming to some extent the problems caused by poor transfer efficiency of these devices. The detectors are isolated islands connected to the column CCD shift register by a transfer gate. The signal charge is transferred to the column register during the application of the transfer pulse; therefore, the array can be integrating input flux while the results of the previous integration are being read out. During readout, the signal charge is detected by a floating diffusion charge amplifier.

II. Experimental Results

A. Test Geometry

The imaging system used for both laboratory and telescope tests consisted of a cryostat assembly, signal processing electronics, and a computer system as shown in detail in Fig. 3. The cryostat system consisted of a commercial Janis LN_2 research Dewar that contained the PtSi Schottky barrier CCD and a cooled interference filter. The bandpass of the filter was 2.0–2.4 μm (K band); the filter was cooled to 77 K to eliminate any background radiation from the filter itself since the detector responds to beyond 4 μm. The K band was chosen for these tests because of the higher quantum efficiency of the detector, the astronomical interest in imaging in the 2-μm band, and the ease of testing in the laboratory. The signal processing electronics consisted of an analog processor, digital control logic to generate the clock signals, and a frame grabber. The analog processor utilized a double correlated sampling system to remove the reset (KTC) noise and a 12-bit ADC to digitize the data for entry into the frame grabber. The frame grabber consisted of a two-port 2048 by 12-bit RAM memory that was used to store one frame on command. It was then possible to read out this memory into the computer system for further data processing. The computer system consisted of a Varian 620/f computer with a disk and tape drive for mass storage. The computer was linked to a Camac system that was the control and data transfer link between the computer and the signal processor. This is a common technique utilized at Kitt Peak to link observing instruments to the computer systems.

B. Telescope Tests

The measurements discussed in this section were made at the Kitt Peak National Observatory using the 1.3-m telescope. The LN_2 cryostat containing the PtSi array was mounted at the Cassegrain focus as depicted in Fig. 4. The f/14 beam of the telescope yields an image scale of 11.3 sec of arc mm^{-1}, so an individual pixel subtends ~0.6 sec of arc. This gave considerable oversampling of the 2–3-sec of arc images encountered during the night of these observations.

The Varian 620/f computer and Camac I/O modules were used for controlling and driving the telescope as well as for the acquisition and processing of the data

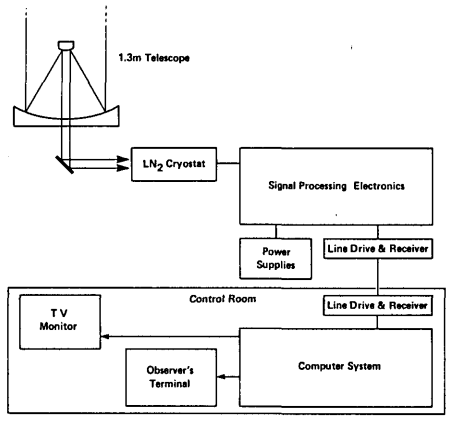

Fig. 4. Block diagram of test geometry utilized at the 1.3-m telescope.

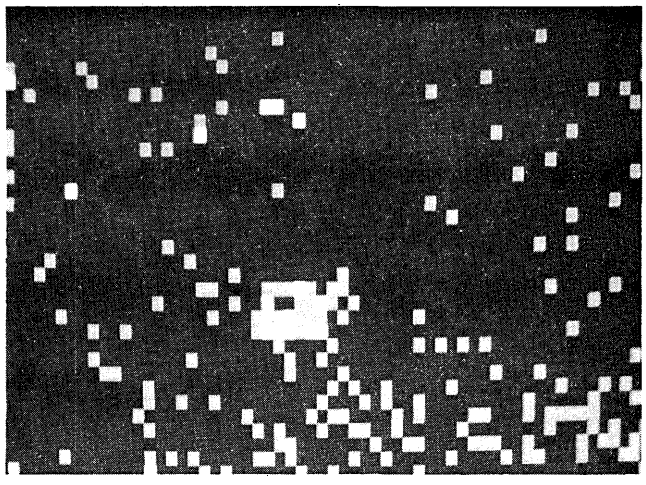

Fig. 5. Photograph of video monitor display showing the star θ Leo with background subtracted. Total integration time was 12.8 sec. Because of the unequal pixel spacing of the array, all the photographs are compressed by a factor of 2 in the horizontal (32-pixel) direction.

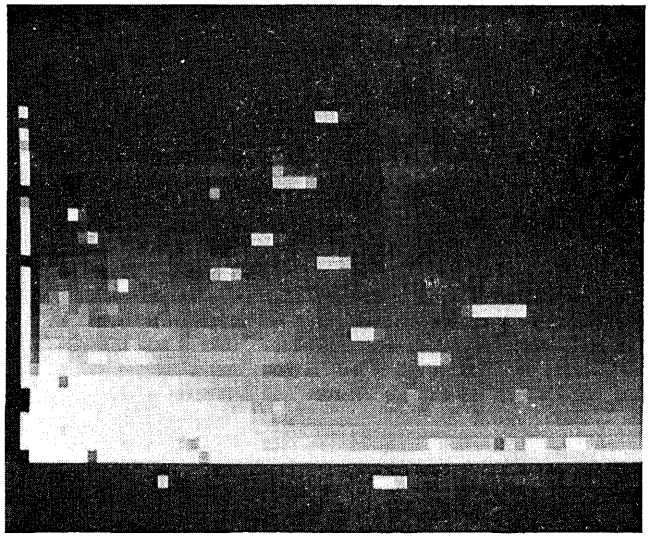

Fig. 6. Photograph of a bright star image before background was subtracted.

from the array. Due to the interrupts needed for telescope control, the array in the frame grabber was read out approximately once per second. These data were then added to the data already stored on a pixel-by-pixel basis, while a new array of data entered the frame grabber. After proper scaling at the end of the data acquisition cycle, this array became the average data frame, which was then stored on disk and magnetic tape. Each pixel of this array is the average of the corresponding pixel in the data sequence of several frames.

Using this technique, an average object-plus-background frame of data was computed and stored using up to 100 frames of raw data with the telescope pointed at an object. An average background frame was computed in the same manner, with the telescope pointing at a nearby blank sky field. The difference between these two averaged data frames was computed and saved as object data. These three data frames were then available for computer analysis at the off-site facility.

The photograph shown in Fig. 5 of the star θ Leo (magnitude +3.5 with in-band flux density of $\sim 5 \times 10^{-16}$ W/cm^2 at the focal plane) was taken from a video monitor display of the object data frame, where the contrast of the picture was enhanced by expanding the dynamic range of interest using an 8-bit digital scan converter adjusted for both brightness and contrast. Figure 6 shows a photograph of a star image without background subtraction, and Fig. 7 shows the same star with the background subtracted. This clearly illustrates the image enhancement due to background subtraction. Figure 8 shows a lunar crater image obtained using background subtraction.

These preliminary results are sufficiently encouraging to indicate that an array using the PtSi technology could be a useful managing device for IR astronomy. The instrumentation used in this evaluation, while sufficient for laboratory testing, proved inadequate to withstand the observatory environment. The detector temperature fluctuated considerably as the telescope attitude was changed, evidently due to imperfect thermal coupling of the LN_2 to the cryostat work surface. The drive and output signal handling electronics exhibited considerable dc drift and instability in the cold environment of the telescope dome. Installation of a heater in the electronics enclosure helped maintain the electronics at a suitable temperature for operation but did not entirely eliminate the problems. The device dark current remained sufficiently high to limit our useful integration time to 128 msec, rather than the 1 sec (or more) which would be desirable for astronomy. Tests to investigate the expected drop in dark current with reduction in temperature are being planned. Further electronics optimization should include a higher-resolution ADC and a reduction of excess read noise by means of more careful circuit design, construction, and temperature stabilization.

Proper optical matching of the telescope image to the pixel size would yield appreciable performance gain with respect to imaging applications. Since the integration

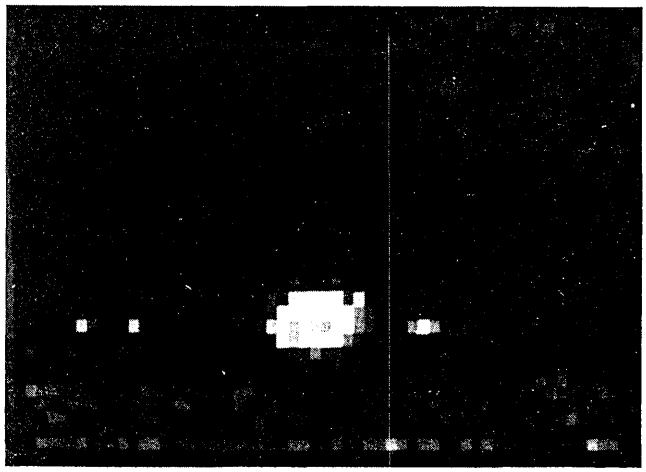

Fig. 7. Photograph of same star as in Fig. 6, with background subtracted.

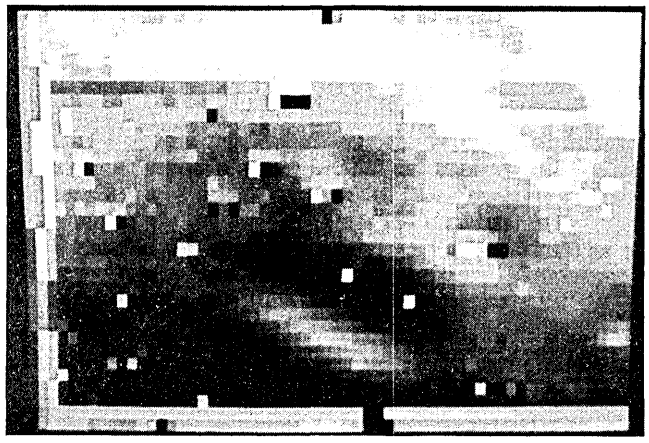

Fig. 8. Photograph of lunar crater image with background subtracted.

time with this array is limited by dark current saturation, it is desirable to match the seeing disk of a point source (typically 2–3 sec of arc at this telescope) to the pixel size. During these tests, no attempt at optical matching was made, with the result that an individual pixel subtending 0.6 arcsec received perhaps 4% of the radiation from a point source. For the star θ Leo, the estimated incident flux on the pixel at the center of the image was 1.8×10^5 photons during the 128-msec integration time.

Aside from anticipated gains in performance resulting from lower noise readout circuitry, one could expect to improve the detectivity of the present array by a factor of 100 for astronomical imaging applications by proper optical matching and reducing the dark current to allow integration times of the order of 1 sec. The poor filling factor of the present array would be a serious problem when used with a reduced-scale image, particularly because of the large dead space between the columns. This could be alleviated by improved array design or by shifting the image by half the column spacing between frames and interleaving the output to produce a 64 ×

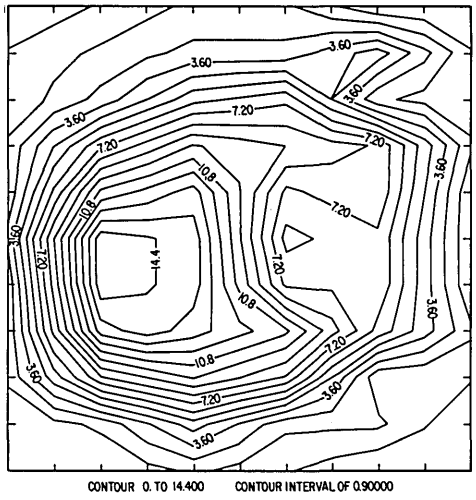

Fig. 9. Intensity contour plot of the image of the object CIT-6 with background subtracted. The tick marks on the coordinate axes represent the pixel spacing in the vertical direction. The horizontal data points were interpolated to correct for the unequal array pixel spacing and make the plot a true representation of the focal plane.

64 image frame. This could be done easily on any telescope with a programmable secondary mirror.

Observations made on CIT-6, which is a strong IR source, were further analyzed to determine quantum efficiency and general performance characteristics of the array. Figure 9 is an intensity contour plot of CIT-6. The effects of the poor transfer efficiency of this array can be seen in the compression of the contours of the leading edge of the star image and the spreading of the contours on the trailing side. The effect of the transfer inefficiency is much more pronounced in the horizontal than in the vertical register. This is a typical result that we have seen on numerous other CCD type imagers and is probably due to the higher shifting speed of the horizontal register. There is a dummy pixel between each vertical column that could be used to improve the transfer results by adding the contents of that cell, which should be zero under ideal conditions, to the previous cell in the video data. This was not done for these tests because the frame grabber was not designed to save the contents of the dummy pixel.

A numerical integration was performed on the contour plot to determine the total power collected from the source CIT-6, and this was compared with the known power from this source. This measurement resulted in a quantum efficiency of ~0.4% for the array including the dead space or ~1.8% for the active area only. These numbers compare favorably with the laboratory measurements and are consistent with previous measurements made on this type of array.[10]

C. Laboratory Tests

Both before and after the telescope run, tests were conducted in the Kitt Peak National Observatory R&D laboratory in Tucson to calibrate and evaluate the system under repeatable conditions. The parameters thus investigated were system conversion gain, noise,

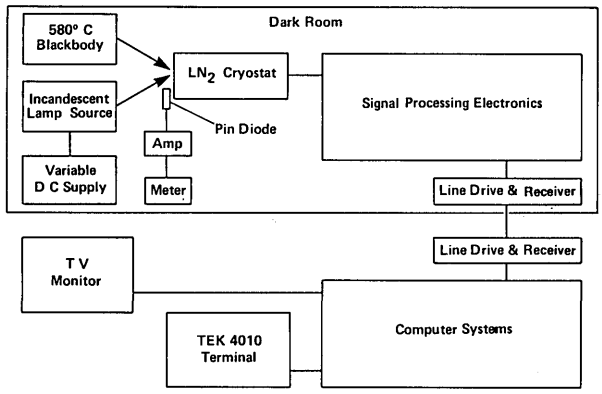

Fig. 10. Block diagram of the laboratory test geometry.

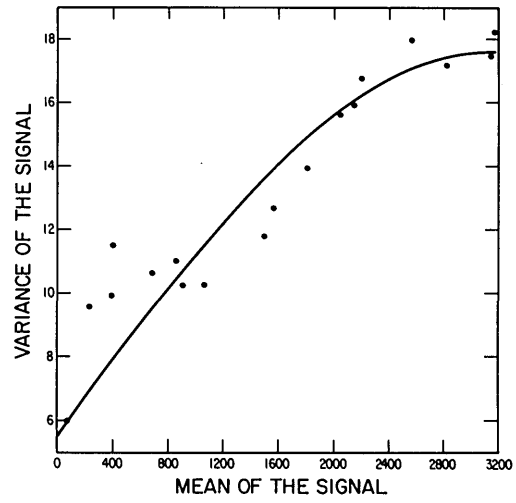

Fig. 11. Mean-variance plot obtained by laboratory tests.

linearity (both large and small signal), and dynamic range. To make the results more meaningful, a subset of 635 pixels of the 2048 available pixels was used for analysis. These pixels were selected on the basis of response uniformity and freedom from extreme noise artifacts. A block diagram showing the laboratory test setup is shown in Fig. 10.

1. *System Conversion Gain and Noise*

Basic to the evaluation of any imaging sensor is the determination of the system conversion gain and read noise. Many times this is estimated, but it can in fact be quantitatively determined based on the following relationship:

$$V(s) = n^2 g^2 + \bar{s}g, \tag{4}$$

where $V(s)$ is the output noise variance in digital units due to input photon flux s,
g is the system gain in digital units/input electron,
n is the system rms noise in electrons, and
$\bar{s}$ is the mean output signal in digital units due to input photon flux s.

Implicit in the use of this relationship, herein referred to as the mean-variance curve, is the assumption that the only sources of noise are the quantum noise associated with the signal and the signal amplitude independent system noise. This relationship is commonly used in the evaluation of visible CCDs,[11] and its derivation can be found in a paper by Mortara and Fowler[12] on the evaluation of CCDs for astronomical use. Digital units (du) are used here because most data are taken after A–D conversion for reduction by computer, but the measurements can just as easily be made in the analog domain. This equation is a straight line whose y intercept is the system noise and slope is the system conversion gain. In addition, the system full scale or well capacity can be determined where this curve departs from a straight line at the higher signal levels. Any other departure of this curve from a straight line is an indication of a nonlinear system response.

The data to generate each point on the curve consisted of ten exposure frames, typically at an integration time of 16 msec, at some input flux level (the level need not be known but must be stable during the exposure period), and ten frames at the background level. It is necessary that the background level be near zero or errors will occur in computing $\bar{s}$. From these data an average signal plus background and average background frame are computed, and an average exposure frame is determined from their difference. The average signal $\bar{s}$ is determined by computing the mean of the selected 635 pixels in the average exposure frame. The determination of the variance $V(s)$ is somewhat more complicated. First, to eliminate the coherent features, the average signal plus background frame is subtracted from each of the ten signal plus background frames to create ten noise frames from which the variance is computed using the selected 635 pixels. The Gauss correction factor of 10/9 is then applied to the result.

The mean-variance curve obtained on this device is shown in Fig. 11. From this curve it is obvious that there is a linearity problem at levels below 900 du, which was also seen in the small signal linearity tests discussed later. It was noted that the signal level in the dummy pixel also rose with flux level during this period. It is thought that the nonlinearity is caused by charge being lost from the signal to the dummy pixel at low flux levels due to poor charge transfer efficiency. Since this would be a noisy process, it could account for the increase in the variance. This explanation is further strengthened by the fact that the straight-line projection of the linear part of the curve at higher flux levels intersects the y axis with the measured zero flux measurements. Also, one would not see this effect in the measured value for the zero flux case if the plateau in the variance were simply due to dark current noise. Although this array utilizes a buried channel CCD and one would not expect this effect, it may in fact be caused by the low operating temperature (77 K) requirement of the array. Introducing and optimizing an electrical fat-zero signal or signal processing techniques utilizing the contents of the dummy pixel should reduce this effect.

To obtain the system conversion gain we did a linear

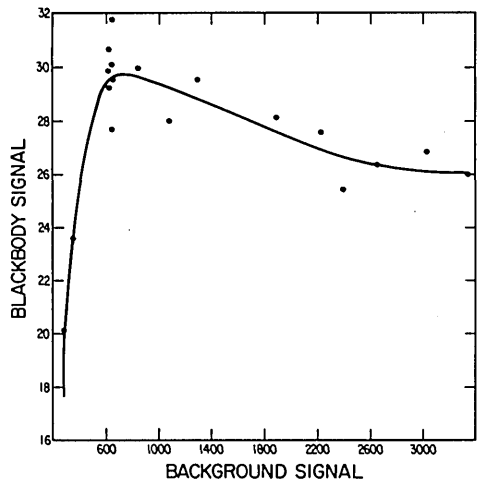

Fig. 12. Small signal linearity plot obtained in the laboratory.

regression using the data from the midrange area of this curve and obtained a gain of $\simeq$180 electrons/du. Using this gain, a saturation level of 400×10^3 electrons was computed. The read noise in the zero flux case was $\simeq$400 electrons, resulting in a dynamic range of $\simeq 10^3$ if one ignores the problem area at low signal levels. These data were taken before and after the telescope test, and the results compared favorably, indicating that the signal processing electrons were stable under laboratory conditions.

2. *Small Signal Linearity*

In these measurements we evaluated the intensity of the system as a function of background flux. This is important since sky and dark current background signal are much larger than the desired signal. The test consisted of varying the background flux with a lamp source and generating a stable small signal utilizing a 580 K blackbody source. To reduce the system noise effects, twenty-five frames of data were averaged utilizing the same 635 pixels as in the previous measurements. The average frame of signal plus background was subtracted from the average background frame to obtain the signal level. A plot of signal level vs background level from this test is shown in Fig. 12.

Like the mean-variance curve, this plot shows the gain reduction at lower background signal levels. The small signal linearity in the midrange shows a general decrease in gain, which is possibly due to the increase in the negative charge on the PtSi electrode or to the resultant decrease in bias voltage level. Further study and testing are required to verify this theory.

3. *Quantum Efficiency*

To verify the telescope measurements, the quantum efficiency was measured in the laboratory. A blackbody was used as the known source of flux. The conversion gain measured previously was used to determine the number of electrons for the calculation. The signal level was determined from the difference between an averaged signal plus background frame and background frame. The quantum efficiency measured in this manner was 2.3% for the active area. If one takes into account the filling factor, the array quantum efficiency is 0.5%, which compares favorably with the telescope measurement of 0.4%. The array being evaluated was a couple of years old; recent improvements in technology are believed to result in detectors with an order of magnitude improvement in quantum efficiency.

III. Conclusions

The results of the preliminary investigation indicate that PtSi Schottky technology has potential as an imaging array in the 2–2.5-μm band. Several of the problems discovered in the preliminary evaluation will have to be solved or better understood so that the calibration procedures can be developed. The quantum efficiency and filling factor problems have been addressed by recent improvements in the Schottky barrier technology, which are yielding quantum efficiencies of 20 and filling factors over 90%. A redesign of the electronics could correct the temperature problems at the telescope and provide additional flexibility in signal processing. The low-level transfer efficiency problem can be improved by utilizing the signal in the dummy pixel, introducing a fat zero in the present design, or by designing an improved CCD tailored for operation at 77 K. The gain change with background will have to be investigated more carefully so that its effect can be predicted.

With these improvements, it should be possible to increase the sensitivity of a Schottky barrier imager by a factor of 100 or more from the 3.5 magnitude level achieved in this investigation. Although these arrays are a long way from the sensitivities of single or multiple discrete detectors in the band, the 2-D format will be a useful addition in those intensity ranges where there is sufficient flux.

We wish to acknowledge helpful discussions with F. Shepherd of Rome Air Development Center. This work was partially supported by Defense Advanced Research Projects Agency and Air Force Office of Scientific Research. The contract was monitored by Rome Air Development Center ESE.

Kitt Peak National Observatory is operated by the Association of Universities for Research in Astronomy, Inc. under contract with the National Science Foundation.

References

1. B. R. Capone, R. W. Taylor, and W. F. Kosonocky, Opt. Eng. 21, 5 (Sept./Oct. 1982).
2. B. R. Capone *et al.*, Opt. Eng. 18, 5 (Sept./Oct. 1979).
3. W. Kosonocky, "Schottky Barrier Infrared Charge-Coupled Device Focal Plane Arrays," Proc. Soc. Photo-Opt. Instrum. Eng. 443, 167 (Aug. 1983).
4. F. Shepherd, "Schottky Diode Infrared Detectors," Proc. Soc. Photo-Opt. Instrum. Eng. 443, 42 (Aug. 1983).

5. F. D. Shepherd and A. C. Yang, "Silicon Schottky Retinas for Infrared Imaging," in *Proceedings, International Electron Devices* (1973), pp. 310–313.
6. C. H. Sequin and M. F. Tompsett, *Charge Transfer Devices* (Academic, New York, 1975).
7. V. E. Vickers, Appl. Opt. **10,** 2190 (1971).
8. M. Kimata, M. Denda, T. Fukunoto, N. Tsubouchi, S. Uematsu, H. Shibata, T. Higuchi, T. Sahehi, R. Tsunoda, and T. Kanno, Jpn. J. Appl. Phys. **21,** Suppl. 21-1, 231 (1982).
9. J. D. E. Beynon and D. R. Lamb, *Charge Coupled Devices and Their Applications* (McGraw-Hill, New York, 1980), p. 27.
10. W. F. Kosonocky, H. Elabd, and H. G. Erhardt, RCA Eng. **27,** 42 (May/June 1982).
11. A. M. Fowler, P. Waddell, and L. Martara, Proc. Soc. Photo-Opt. Instrum. Eng. **290,** 34 (1980).
12. L. Mortara and A. M. Fowler, Proc. Soc. Photo-Opt. Instrum. Eng. **290,** 28 (1980).

Astronomers continued from page 837

In between stretches the hefty, 20-foot-long, 4-foot-diameter chamber of the normal incidence vacuum spectrometer used to analyze molecular radiation. Here, too, is a 12-foot-long shock tube, a vacuum Mach-Zehnder interferometer and the microwave line-width measuring apparatus now under construction. Surrounded by orderly arrays of snakelike hoses, racks of blinking electronic equipment and clusters of electrical wiring, several of these experiments could easily fill an average American home. Even the smallest would take over the garage.

Harvard astrophysicist Bartley Cardon explains the operation of the aerodynamically driven shock tube, a stainless-steel pipe standing chest-high at right angles to the vacuum spectrometer. "In one part of the tube we have the 'driver'—hydrogen gas at a pressure of 700 pounds per square inch. Two aluminum diaphragms separate the driver from the 'test' gas, typically neon or argon, which is at very low pressure."

"Mixed in with the test gas is the element whose spectrum we really want to study—in this case, cobalt, in the form of a volatile compound. When we discharge the gas between the two diaphragms, the hydrogen driver causes the diaphragms to rupture, producing a shock wave through the test gas. This shock wave finally heats up the test gas to about 12,000 degrees. Although this happens just for an instant—typically 1/1000 of a second—it is time enough to photograph the ultraviolet spectrum of the resulting cobalt vapor."

Subsequent analysis of the cobalt spectrum will help astronomers understand so-called Type I supernova explosions, believed by some to originate in stars one to four times more massive than the sun. Indeed, radiation emitted by excited cobalt ions probably accounts for many features seen in the spectra of such supernova outbursts.

Upstairs, above the shock tube, theorist George Victor sits at a desk covered with papers bearing equations from advanced quantum physics. Victor notes that some aspects of astronomical research are very difficult to conduct in the lab. "For example, take studies of the OH or hydroxyl molecule, one of the molecules seen in interstellar space. It's highly reactive and therefore tough to handle. That's where theoretical calculations can play an important role. Work by Alexander Dalgarno and Jeng-Hwa Yee [at the Center for Astrophysics] has shown that the OH molecule is probably responsible for the strange glow that was observed around the unmanned Atmospheric Explorer Satellite several years ago."

This glow had puzzled astronomers for some time. The quantum calculations provided an answer: Oxygen atoms picked up by the unmanned explorer satellite as it rammed into the very thin atmosphere of low-Earth orbit combine with vagabond hydrogen atoms to form the OH molecule. Observations of the aura around the spacecraft were consistent with the spectrum calculated for the OH molecule. And, the intensity of the glow was seen to vary closely with atmospheric concentrations of oxygen as the satellite ranged between the high and low points of its orbit.

The NASA Space Shuttle also glows in the dark. "We thought initially that the same OH process was at work around the shuttle," Victor says. "But it didn't work out that way. Analyses of pictures of the glowing shuttle tail section taken by the crew yield lifetimes of the radiating molecules that are different from the lifetimes of OH molecules. So it's back to the drawing board."

The shuttle glow thus remains a mystery. "It would be a big help," Victor says, "if we could get spectral observations of the shuttle glow from the ground. Unfortunately, only one big telescope can track fast enough to follow the shuttle across the night sky—the Multiple Mirror Telescope [operated by the Smithsonian Institution and the University of Arizona on Mount Hopkins, in Arizona]—and the MMT is too far north to see the shuttle high above the horizon, given the orbits now being flown. Perhaps, when the shuttle begins to be launched from California as well as from Florida, we can clear up this mystery."

Across the hall from Victor's office, theorist Jane Fox readies another computer run. Like many astronomers who don't use telescopes, Fox was not trained in astronomy; she was originally a chemist. But, unlike her colleague George Victor, she doesn't study individual atomic processes. Her main activity today is modeling—constructing mathematical representations of the martian atmosphere to determine the concentrations of various ions and molecules at various heights above the planet's surface. With the computer, Fox can then take a trip—mathematically—back in time and calculate how the atmosphere might have evolved under the influence of the sunlight falling on Mars.

Fox was converted to atmospheric science from chemistry through discussions with Alexander Dalgarno, one of the leaders in the field. "When I began this work in the 1970s," Fox explains, "it made sense to start with the atmospheres of Venus and Mars. Since there were spacecraft going to those planets, you could get back direct observational data to check your models.

"Venus provided one of my most satisfying suc-

continued page 900